

ACCRETION AND OUTFLOW IN THE AGN AND STARBURST OF NGC 5135

N. A. LEVENSON¹, K. A. WEAVER^{2,3}, T. M. HECKMAN³, H. AWAKI⁴, AND Y. TERASHIMA⁵

To appear in ApJ Vol. 602, Feb. 10 2004

ABSTRACT

Observations of the Seyfert 2 and starburst galaxy NGC 5135 with the *Chandra X-ray Observatory* demonstrate that both of these phenomena contribute significantly to its X-ray emission. We spatially isolate the active galactic nucleus (AGN) and demonstrate that it is entirely obscured by column density $N_H > 10^{24} \text{ cm}^{-2}$, detectable in the *Chandra* bandpass only as a strongly reprocessed, weak continuum and a prominent iron $K\alpha$ emission line with equivalent width of 2.4 keV. Most of the soft X-ray emission, both near the AGN and extending over several-kpc spatial scales, is collisionally-excited plasma. We attribute this thermal emission to stellar processes. The AGN dominates the X-ray emission only at energies above 4 keV. In the spectral energy distribution that extends to far-infrared wavelengths, nearly all of the emergent luminosity below 10 keV is attributable to star formation, not the AGN.

Subject headings: Galaxies: individual (NGC 5135) — galaxies: Seyfert — X-rays: galaxies

1. INTRODUCTION

Active galactic nuclei and star formation are fundamentally related. In their quiescent states, black hole and stellar components are observed to be related in individual galaxies in the rough proportionality between the black hole mass and the velocity dispersion of the stellar spheroid (Gebhardt et al. 2000; Ferrarese & Merritt 2000), suggesting a connection over cosmological timescales. Also, Kauffmann et al. (2003) find a strong connection between active galactic nucleus (AGN) luminosity and the age of the stellar population of the host galaxy for AGNs in the Sloan Digital Sky Survey. Locally, AGNs and strong star formation are correlated, with roughly half of well-selected samples of Seyfert 2 galaxies exhibiting compact circumnuclear starbursts (Cid Fernandes et al. 2001, and references therein). These Seyfert 2/starburst composite galaxies contain genuine AGNs, which accretion onto the central black hole powers, but the stellar processes can also become energetically significant.

The local composite galaxies afford detailed examination for discrimination of their AGN and stellar contributions and accurate measurement of these combined effects. The detailed studies serve as an important foundation for understanding ultraluminous infrared galaxies, whose bolometric luminosities exceed $10^{12} L_\odot$ (Sanders & Mirabel 1996). Among this class, the problem is to identify either an AGN or star formation as the primary energy source. If present, an AGN may be deeply buried, obscured both on small scales associated directly with the central engine and on the large scales of star formation (Ptak et al. 2003). While the composite galaxies are not the direct analogues of these com-

plex higher-luminosity cases, they serve as basic building blocks, demonstrating the primary consequences of combining starbursts with AGNs in highly obscured circumstances.

Distinguishing these X-ray emission processes is also important in the study of the cosmic X-ray background (XRB). AGN can fundamentally produce the XRB (e.g., Giacconi et al. 2001), but they require a distribution of redshift and absorption to match its observed spectrum (e.g., Setti & Woltjer 1989). The outstanding difficulty is to identify the highly-obscured populations, which are not always evident at energies below 10 keV. The Seyfert 2/starburst composite galaxies cannot directly account for the XRB, but they tend to be strongly obscured (Levenson, Weaver, & Heckman 2001a), and they illustrate the systematic effects of observing AGNs in the presence of starbursts, even at X-ray energies.

With high spatial resolution and simultaneous spectroscopic data from the *Chandra X-ray Observatory*, we analyze here the X-ray emission due to both AGN and starburst components of the Seyfert 2/starburst composite galaxy NGC 5135. This galaxy is optically classified as a Seyfert 2 on the basis of emission line ratios (Phillips, Charles, & Baldwin 1983). It also contains a powerful starburst within 200 pc of the nucleus that is most evident at ultraviolet energies (González Delgado et al. 1998). NGC 5135 is relatively nearby, at distance of 59 Mpc (assuming $H_0 = 70 \text{ km s}^{-1} \text{ Mpc}^{-1}$), so $1''$ corresponds to 285 pc. In X-rays, we expect to find the characteristic unresolved non-thermal continuum from accretion onto the central black hole (Turner et al. 1997). We also distinguish the dominant X-ray signature of a starburst: spatially extended thermal emission, due to individual supernovae and stellar winds, which collectively may produce a “superwind” outflow that escapes the galaxy (Dahlem, Weaver, & Heckman 1998). With the simultaneous spatial and spectral distinction of these emission processes, we can more accurately measure them independently. Relating the X-ray data to multi-wavelength observations of this galaxy as a whole, we draw general conclusions about identifying multiple energy sources

¹ Department of Physics and Astronomy, University of Kentucky, Lexington, KY 40506; levenson@pa.uky.edu

² Code 662, NASA/GSFC, Greenbelt, MD 20771

³ Department of Physics and Astronomy, Bloomberg Center, Johns Hopkins University, Baltimore, MD 21218

⁴ Department of Physics, Faculty of Science, Ehime University, Bunkyo-cho, Matsuyama, Ehime 790-8577, Japan

⁵ Institute of Space and Astronautical Science, 3-1-1 Yoshinodai, Sagami-hara, Kanagawa 229-8510, Japan

in low-resolution observations of galaxies that contain AGNs.

2. OBSERVATIONS AND DATA REDUCTION

The *Chandra* Advanced CCD Imaging Spectrometer (ACIS) observed NGC 5135 on the back-illuminated S3 detector on 2000 September 4. (See Weisskopf et al. 2000 for more information on *Chandra*.) We reprocessed all data from original Level 1 event files removing the spectral and spatial randomization that is included in standard processing with *Chandra* Interactive Analysis of Observations (CIAO) software. We applied the current gain corrections for the S3 CCD (from 2001 July 31), and we included only good events that do not lie on node boundaries, where discrimination of cosmic rays is difficult. We examined the lightcurves of background regions and found no significant flares, so we used all data within the standard good-time intervals, for a total exposure of 29.3 ks.

3. IMAGE ANALYSIS

These *Chandra* data reveal the complexity of NGC 5135's X-ray emission, as we illustrate with the total 0.4–8.0 keV image (Figure 1). The raw ($0''.5$) pixels have been smoothed by a Gaussian of $\text{FWHM}=1''.5$, and both the image intensity and contours are scaled logarithmically. The active nucleus is not the only source of X-rays. Rather, the image reveals diffuse emission, off-nuclear point sources, and, most surprisingly, *two* bright central sources, separated by $2''$. As we demonstrate below, only the northern of these two is the active nucleus. The highly-smoothed version of the image (Figure 2), shows that the soft emission extends over a scale of approximately $50'' \times 30''$ ($14 \text{ kpc} \times 9 \text{ kpc}$), tracing the large-scale bar in the disk of NGC 5135.

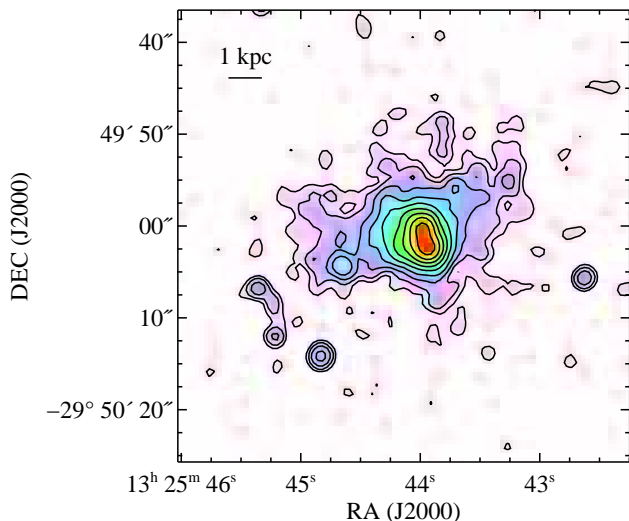


FIG. 1.— *Chandra* X-ray image of NGC 5135. The broad-band (0.4–8 keV) image has been smoothed by a Gaussian of $\text{FWHM}=1''.5$. The image is scaled logarithmically. The overlaid intensity contours begin 6σ above the background level and increase by factors of two. The AGN is the northern central source, while the starburst is responsible for the southern nuclear concentration and diffuse emission. Several additional sources are also apparent.

We consider three broad energy regimes separately: 0.4–1.0, 1.0–4.0, and 4.0–8.0 keV, which we refer to as the soft, medium, and hard images. In soft X-rays, (Figure 3), the galaxy appears very similar to the total image. The very extended emission is soft, and both central sources are evident. Some of the additional sources toward the east are less prominent or do not appear at lower energies. Some of the extended emission is still detected in the medium X-ray (1–4 keV; Figure 4) image, and the additional sources are more prominent. In hard X-rays (4–8 keV; Figure 5), the northern central source is strongest. The southern source contributes weakly, but is still evident, and two of the eastern sources are significant.

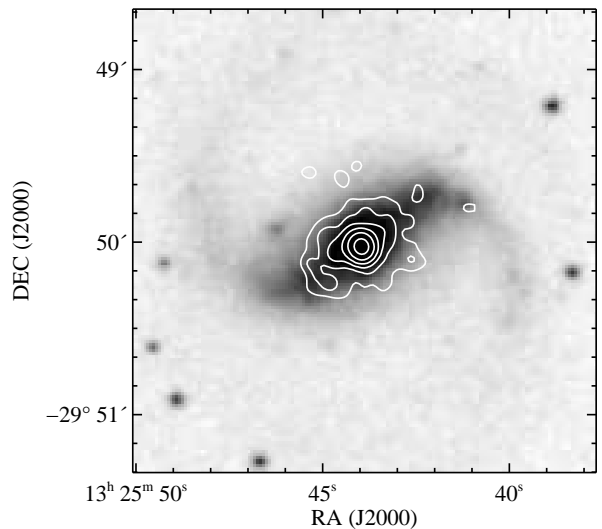


FIG. 2.— Digitized Sky Survey red image with 0.4–8.0 keV X-ray contours overlaid. The X-ray data have been smoothed by a Gaussian of $\text{FWHM}=5''$ to illustrate the correlation of X-ray and optical emission on large scales. The optical image is scaled linearly, and the X-ray contours are scaled logarithmically.

We compare the two central sources with *Chandra*'s point-spread function (PSF) in the three separate energy bands. In each of these three bands, we model the emission profile as a constant plus two two-dimensional Gaussians having circular cross-sections. In all cases, the Gaussians are significantly broader than a similar two-dimensional fit to the PSF at the appropriate energy and detector position modeled with the CIAO task *mkpsf*. We conclude that the two central sources are resolved in all three broad bands. Therefore, neither of the broad-band emission peaks is due to the unresolvable AGN alone.

We do, however, morphologically identify the AGN in the Fe $K\alpha$ emission of NGC 5135. This fluorescent line radiation arises near the strong AGN continuum and advantageously avoids confusion with the soft, thermal starburst. In this case, the Fe line is prominent above the continuum that either the AGN or other sources could produce. Isolating the emission in the 5.5–7.5 keV band-pass and subtracting the continuum measured from 4 to 5.5 keV produces an image in Fe $K\alpha$. This image contains an unresolved point source, which is located $0''.5$ north of the northern emission peak that is measured in

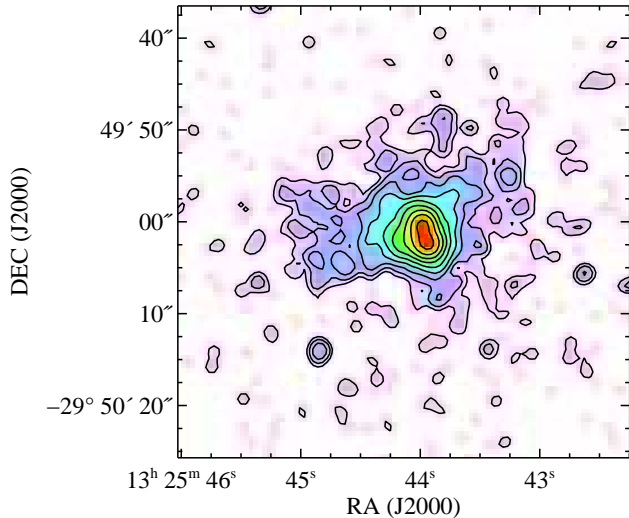


FIG. 3.— *Chandra* soft X-ray (0.4–1 keV) image of NGC 5135, smoothed by a Gaussian of FWHM=1''.5. The image is scaled logarithmically. The overlaid intensity contours begin 8σ above the background level and increase by factors of two.

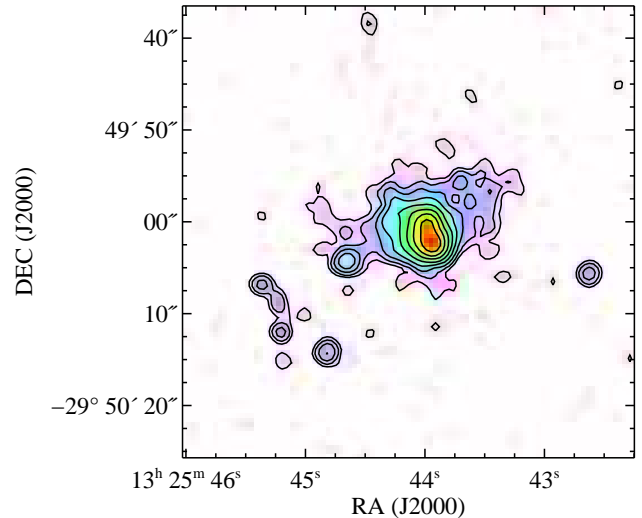


FIG. 4.— *Chandra* medium X-ray (1–4 keV) image of NGC 5135, smoothed by a Gaussian of FWHM=1''.5. The image is scaled logarithmically. The overlaid intensity contours begin 6σ above the background level and increase by factors of two.

the total band image. Thus, the Fe $K\alpha$ image specifically locates the AGN on the northern side of the broad peak that appears in the total band image, with both the AGN and other sources contributing to the spatially-extended broad-band peak. At the distance of NGC 5135, the point-like morphology constrains the physical scale of the Fe $K\alpha$ emission to $R \lesssim 285$ pc.

4. SPECTROSCOPY

We extracted spectra from several interesting regions. In all cases, we also measured the local background in nearby source-free regions and subtracted it. Over the course of the *Chandra* mission, the soft X-ray sensitivity has diminished, likely the result of build-up of material on the detector. We have used the “ACISABS” model of G. Chatras and K. Getman⁶ to create ancillary response files that account for this time-varying effect. In general, we grouped the spectra into bins of a minimum of 30 counts, so χ^2 statistics are appropriate in the model fitting, which we performed in XSPEC (Arnaud 1996). In the best-fitting models discussed below, only data from 0.4 to 8.0 keV are considered, and the inclusion of additional model components and their free parameters are significant at a minimum of the 95% confidence limit, based on an F test. All quoted errors are 90% confidence for one parameter of interest.

Observational results from “pure” AGN and “pure” starbursts physically motivate the spectral models we consider, and we recognize that all components may be present here, even in spatially-restricted regions. The AGN produces an X-ray continuum that is characterized by a power law of photon index $\Gamma \approx 1.9$, as observed in Seyfert 1 galaxies (Nandra & Pounds 1994), assuming the central engines of Seyfert 1s and Seyfert 2s are intrinsically identical. With modest column density along the line of sight, the soft X-rays will be photoelectrically

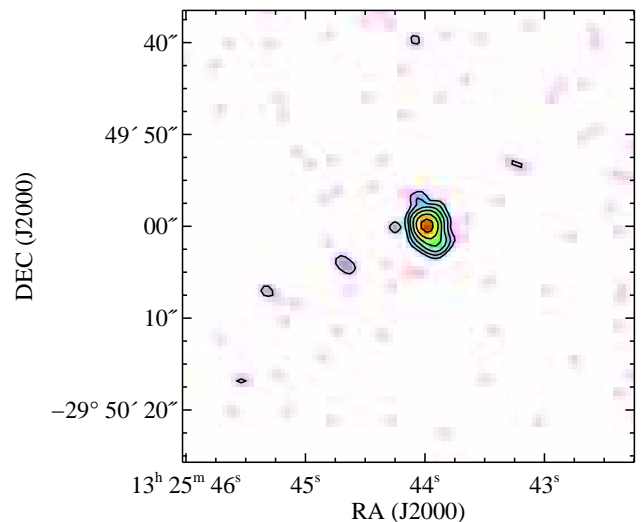


FIG. 5.— *Chandra* hard X-ray (4–8 keV) image of NGC 5135, smoothed by a Gaussian of FWHM=1''.5. The image is scaled logarithmically. The overlaid intensity contours begin 8σ above the background level and increase by factors of two. The AGN is the strongest source, although resolved emission due to the southern starburst concentration is also evident.

cally absorbed. When the obscuration becomes Compton thick, which is the case here, the emergent continuum is entirely reflected and is strongly reprocessed, to $\Gamma \approx 0$ (e.g., Krolik, Madau, & Życki 1994) within the observed energy regime. Fluorescent Fe emission is common in the X-ray spectra of Seyfert galaxies. The Fe $K\alpha$ line appears at central energy $E_c = 6.4$ keV in material less ionized than Fe XVII. If the iron is nearly fully ionized, $E_c = 6.7$ or 6.9 keV, for He-like or H-like ions, respectively. Each of these fluorescence lines may be spectrally

⁶ <http://www.astro.psu.edu/users/chartas/xcontdir/xcont.html>

characterized by a single Gaussian. The starburst produces X-rays in both point sources and genuinely diffuse gas. Observed starburst spectra tend to be soft, indicating multiple thermal components in the diffuse material as well as a hard continuum (e.g., Dahlem et al. 1998, 2000). The X-ray binaries produce the power-law continuum, although the integrated spectrum of the unresolved sources may not be characteristic of any individual sources.

4.1. The AGN Region

We centered the extraction of the northern central source on the Fe $K\alpha$ center measured in the images. We measured the spectrum in a region of only $1''.2$ radius to avoid contamination by the southern source. The best-fitting model requires two thermal components and a Gaussian at soft energies in addition to a flat power law continuum and a Gaussian line, which are characteristic of the AGN at higher energies. We apply the same absorption by a foreground screen to all of these components. Figure 6 contains the data, model, and ratio of data/model, and Table 1 lists the model parameters. We had previously fit the 4–8 keV spectrum (Levenson et al. 2002) with a power law and a single Gaussian to measure the Fe $K\alpha$ line and its underlying continuum. In order to retain significant information at energies above the line, we fit the unbinned spectrum using the C-statistic (Cash 1979). The Fe line is spectrally unresolved, with equivalent width $EW = 2.4$ keV. The power law is flat ($\Gamma = 0$), characteristic of a pure reflection spectrum. The large EW and flat spectral slope demonstrate that the AGN is not viewed at all directly within the *Chandra* bandpass; it must be obscured by $N_H > 10^{24}$ cm $^{-2}$.

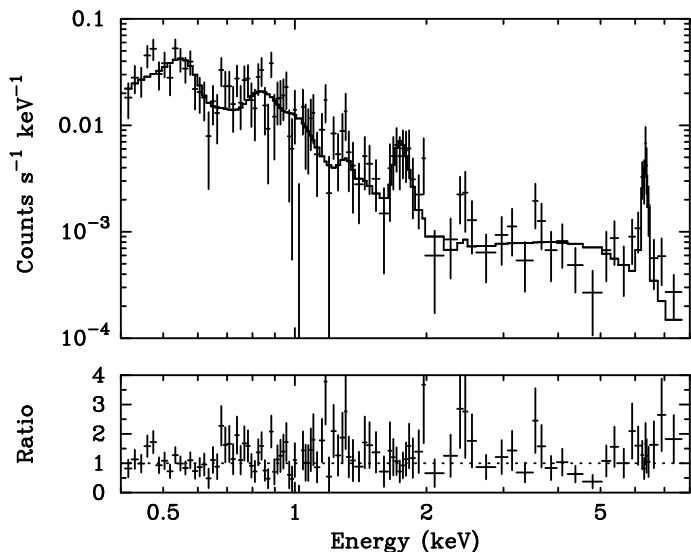


FIG. 6.— *Chandra* ACIS-S3 spectrum of the northern central source. This region includes the NGC 5135 AGN, whose direct X-ray emission is completely obscured. A complex model consisting of two thermal components, a power law, and two emission lines fits the data well. In the upper panel, the data are plotted as crosses, and the model, convolved with the detector response, is plotted as a histogram. The ratio of data/model is plotted in the lower panel.

These results most accurately describe the high-energy emission, so we fix these parameters while fitting the entire 0.4–8 keV binned spectrum. In the complete spectrum, two additional components are

necessary to account for most of the soft X-ray emission. We use the thermal equilibrium model of Mewe and Kaastra (Mewe, Gronenschild, & van den Oord 1985; Arnaud & Rothenflug 1985; Mewe, Lemen, & van den Oord 1986), with updated Fe L calculations (Liedahl 1992) and solar abundance. The two thermal components are at temperature $kT = 0.05$ and 0.6 keV. We note that the normalization of the softer component is several orders of magnitude greater than that of the harder component. The normalization is proportional to the volume integral of the square of the density, and a greatly increased density in the low-temperature region is the likely origin of this difference.

Alternatively, we fit the entire 0.4–8 keV spectrum simultaneously. Again, we use the unbinned data and the C-statistic to retain some information above the high-energy emission line. These parameters are not significantly different from the previous fit and are listed in the second row of Table 1. The slightly steeper photon index ($\Gamma = 0.3$) contributes to the observed 1–2 keV emission, and the high-energy line EW is still large ($EW = 3.0$ keV).

Despite the uncertainties in measuring Γ and its normalization independently, the Fe EW remains large in both the high-energy and full-spectrum fits. Considering the errors on these parameters jointly, a steeper photon index does require a higher normalization (measured at 1 keV), although the magnitude of the high-energy continuum change is small.

The flat power law of the high-energy model is a consequence of reflection. We also considered a more complete model based on Monte Carlo simulations of Compton reflection by a cold population of electrons (Magdziarz & Zdziarski 1995, the PEXRAV model in XSPEC), which further demonstrates that we observe only the reflected continuum and does not improve the fits at all. Specifically, we adopted standard values of the parameters to which we have no sensitivity, fixing the high-energy cutoff $E_c = 100$ keV and inclination angle $i = 63^\circ$. We first considered a fixed intrinsic photon index $\Gamma = 2.0$. Fitting the full spectrum we find the unphysical result that the magnitude of the reflected spectrum relative to the observed intrinsic spectrum exceeds 30, and the Fe $K\alpha$ $EW = 2.9$ keV. The photon index cannot be reasonably constrained. If it is free parameter, we find $\Gamma = 2 (+3, -2)$.

With the spectral resolution and high-energy sensitivity of the present data, there is no discernable difference between a pure reflection model and the simplified flat power law that we have adopted to describe it. Above 4 keV, the only formal difference between these two models is the Fe absorption edge near 7 keV, which we cannot detect. The softer absorption edges of other elements in the reflection model are not strong enough to be detected where thermal emission dominates, despite *Chandra*'s improved sensitivity at lower energies.

We considered the possibility that photoionization by the AGN might produce the soft X-ray emission in the northern region. We attempted to fit the spectrum with photoionization models produced with XSTAR⁷ instead of the thermal plasma components. We also com-

⁷ <http://heasarc.gsfc.nasa.gov/docs/software/xstar/xstar.html>

TABLE 1. SPECTRAL MODEL PARAMETERS

Region	N^a_H	kT^b_1	A^c_1	kT^b_2	A^c_2	Γ	A^d_3	E^e_{line}	EW^f_{line}	$F^{g}_{0.5-2}$	F^h_{2-10}	χ^2/dof
North ⁱ	42^{+33}_{-21}	$0.05^{+0.02}_{-0.01}$	$(3.4^{+24}_{-2.1}) \times 10^4$	0.57 ± 0.09	$3.8^{+0.9}_{-0.6}$	$0.0^{+1.6}_{-0.2}$	$0.21^{+0.04}_{-0.18}$	$6.39^{+0.03}_{-0.04}$	$2.4^{+1.8}_{-0.5}$	$6.1^{+1.5}_{-1.0}$	22 ± 4.4	99/93
...	1.77 ± 0.05	$0.26^{+0.13}_{-0.15}$
North ^j	$21^{+1.2}_{-1.3}$	0.06 ± 0.003	$(1.7^{+0.3}_{-0.2}) \times 10^3$	$0.58^{+0.07}_{-0.09}$	$2.7^{+0.2}_{-0.6}$	$0.3^{+1.3}_{-0.1}$	$0.38^{+0.8}_{-0.1}$	$6.39^{+0.03}_{-0.04}$	$3.0^{+1.4}_{-0.8}$	$6.8^{+0.5}_{-1.4}$	$21^{+2.9}_{-6.8}$	442/509
...	$1.77^{+0.06}_{-0.04}$	$0.17^{+0.15}_{-0.09}$
South	$11^{+5.7}_{-5.0}$	0.66 ± 0.05	$3.8^{+0.8}_{-0.7}$	$2.6^{+0.4}_{-0.3}$	$2.9^{+1.1}_{-0.8}$	11 ± 2	$3.6^{+1.3}_{-0.9}$	39/35
D1	$8.4^{+7.1}_{-3.7}$	0.62 ± 0.07	$2.3^{+0.8}_{-0.6}$	$2.2^{+0.5}_{-0.4}$	1.8 ± 0.6	$7.4^{+2.5}_{-1.9}$	$3.7^{+1.0}_{-1.1}$	39/27
D2	42^{+15}_{-26}	$0.25^{+0.14}_{-0.06}$	$14^{+66}_{-4.7}$	2.2f	0.63 ± 0.3	$3.6^{+2.0}_{-0.9}$	1.2 ± 0.5	21/13

NOTE. — Errors are 90% confidence limits for one interesting parameter. Parameters that are constrained by hard limits are marked with a colon. Fixed parameters are marked with f.

^aColumn density in units of 10^{20} cm^{-2} .

^bTemperature of thermal plasma in keV.

^cNormalization of thermal component in units of $10^{-5} K$, where $K = (10^{-14}/(4\pi D^2)) \int n_e n_H dV$, D is the distance to the source (cm), n_e is the electron density (cm^{-3}), and n_H is the hydrogen density (cm^{-3}).

^dNormalization of power law in units of $10^{-5} \text{ photons keV}^{-1} \text{ cm}^{-2} \text{ s}^{-1}$ at 1 keV.

^eEnergy of line center in keV.

^fEquivalent width of line in keV.

^g0.5–2.0 keV model flux in units of $10^{-14} \text{ erg cm}^{-2} \text{ s}^{-1}$.

^h2.0–10.0 keV model flux in units of $10^{-14} \text{ erg cm}^{-2} \text{ s}^{-1}$.

ⁱParameters and errors on Γ , A_3 , and high-energy components of E_{line} and EW_{line} are based on high-energy fit alone.

^jParameters and errors are based on full spectral fit, using the C-statistic.

pared NGC 5135 with the observed photoionization spectrum of NGC 1068 (Kinkhabwala et al. 2002) because the models fail to reproduce some of the line emission that is detected in this Seyfert galaxy. None of these photoionization spectra accurately reproduce the observed emission of NGC 5135. In general, NGC 5135 exhibits several broad emission peaks that are due to complexes of many unresolved lines, characteristic of thermal emission. Even at the relatively low spectral resolution of these observations, the emission features of all the photoionization spectra appear too sharp.

Finally, in addition to the Fe K line at 6.4 keV and the thermal emission, the northern source also requires a second line at 1.8 keV. This line is consistent with neutral silicon fluorescence, both in central energy and equivalent width (Matt, Fabian, & Reynolds 1997) for the geometry that the Fe emission constrains (§5.2). We searched for other fluorescent lines that are expected to be relatively strong ($EW > 100 \text{ eV}$). The emission measured near 2.4 keV is suggestive of neutral sulfur and can be fit with an unresolved Gaussian of $EW = 340 \text{ eV}$. We caution, however, that this component is not statistically significant in the model fit, and the central energy is significantly (1.8σ) higher than the 2.31 keV expected for sulfur. Some of the lower-energy fluorescent lines, including oxygen, neon, and magnesium, should have large EWs with respect to the reflected continuum, but we cannot discern them against the strong soft thermal emission.

The prominent inner-shell fluorescence lines are characteristic of pure reflection from an optically thick medium. Photoionization of optically thin, low density material does produce line emission, as in the X-ray spectrum of NGC 1068 (Brinkman et al. 2002; Kinkhabwala et al. 2002). In NGC 5135, however, an additional photoionized component would also produce many other strong emission lines, which we do not observe. As we note above, photoionization alone, *instead of* thermal emission, fails to reproduce the soft X-ray spectrum. Alternatively, we consider pure collisional excitation, which does produce some Si line emis-

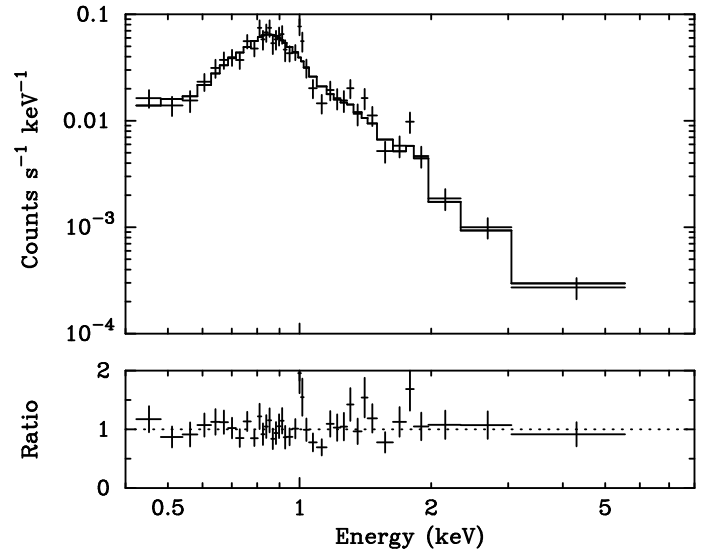


FIG. 7.— *Chandra* ACIS-S3 spectrum of the southern central source, the strong circumnuclear starburst of NGC 5135. Typical of starbursts, the data require a thermal component and a hard X-ray continuum.

sion at similar energies, as observed in other starburst galaxies (Weaver et al. 2002) and Compton thick AGNs (Boller et al. 2003). The line component we model here, however, is required *in addition to* the contributions from the thermal plasmas that are also present and dominate the soft X-ray emission. Thus, we conclude that fluorescent Si is the likely origin of this additional emission line.

4.2. The Compact Starburst

We extracted the spectrum from a region of $1''.2$ radius to isolate the southern central source, which we associate with the strong circumnuclear starburst. The X-ray emission is spatially resolved in all the broad bands measured above. The best-fitting model requires one thermal

component and a power law, both of which are absorbed by the same column density. The temperature of the thermal component is 0.7 keV, similar to pure starburst galaxies. The thermal emission accounts for most of the soft X-rays, and the power law contributes all of the X-ray emission above 4 keV. The extinction along the line of sight, $N_H = 1.1 \times 10^{21} \text{ cm}^{-2}$, is greater than that due to the Milky Way Galaxy alone, although it is comparable to the value González Delgado et al. (1998) measure ($N_H = 9.9 \times 10^{20} \text{ cm}^{-2}$) at ultraviolet wavelengths in a similarly-sized aperture.

The non-thermal power law is likely the net effect of individual sources, primarily X-ray binaries, in the starburst. The slope of the power law is very steep: $\Gamma = 2.6$. Although this is atypical of any individual X-ray binary system, it is characteristic of the integrated spectrum of distinct sources measured in face-on star-forming galaxies, which contain many observable sources (Zezas et al. 2002). We considered fixing the photon index at a value more typical of individual non-thermal X-ray sources ($\Gamma = 1.9$), but found the model fit to the data significantly worse, even allowing for additional soft X-ray components. Figure 7 shows this compact starburst spectrum with the best-fitting model and ratio of data/model, and Table 1 lists the best-fitting model parameters.

4.2.1. Abundance Variations

We also considered thermal plasmas with variable abundances. A starburst wind may be enriched if it carries the metals that supernovae produce. On the other hand, the wind may have low abundances, either because it consists of unenriched halo material or because refractory elements are not present in the gas phase. Low abundances have been reported in X-ray observations of starburst galaxies, but these results may be due to the systematic difficulties of measuring multi-temperature plasmas or neglecting underlying continuum contributions (Weaver, Heckman, & Dahlem 2000; Strickland et al. 2002).

We find slight evidence for non-solar abundances in the southern region of NGC 5135. Considering variable abundances in the thermal component of the best-fitting model above (which includes a non-thermal continuum contribution), the iron abundance is best fit at $[\text{Fe}/\text{H}] = 0.39 (+0.14, -0.13) [\text{Fe}/\text{H}]_\odot$, where $[\text{Fe}/\text{H}]_\odot = 4.68 \times 10^{-5}$ (Anders & Grevesse 1989). We obtain similar results if other refractory elements (Na, Al, Ca, and Ni) are constrained to have the same relative abundance as Fe: $[\text{Fe}/\text{H}] = 0.37 (+0.17, -0.12) [\text{Fe}/\text{H}]_\odot$. The plasma temperature remains the same, although the power law becomes somewhat flatter ($\Gamma = 2.0$). Starburst spectra often show enhanced abundances of alpha elements with respect to Fe (Martin, Kobulnicky, & Heckman 2002; Strickland et al. 2003). Although we cannot simultaneously constrain Fe and alpha abundance variations independently in these data, we do observe this effect generally. Above, varying only Fe abundance, $Z_\alpha/Z_{\text{Fe}} = 2.6 (+1.3, -0.7)$. Alternatively, fixing Fe at solar abundance and allowing the common abundance of O, Ne, Mg, Si, and Ca to vary, $Z_\alpha/Z_{\text{Fe}} = 2.3 (+1.1, -1.0)$, with $\Gamma = 2.3$. The abundance of oxygen most strongly determines the value of this ratio, and here we have adopted $[\text{O}/\text{H}]_\odot = 8.51 \times 10^{-4}$ (Anders & Grevesse 1989).

We also considered multi-temperature thermal plasmas with variable abundances without any non-thermal component. These fits were statistically worse and physically unlikely. Even with the abundance variations, these fits require an extremely high temperature plasma ($kT \approx 10 \text{ keV}$) to account for the emission at energies above 4 keV.

4.3. Diffuse Emission

We extracted two regions of diffuse emission. The first (D1) is the brighter central region of maximum radius $6''.5$, excluding an ellipse that encompasses the extremely bright north and south sources and a point source within the region of interest. The second (D2) is elliptical, extending $14'' \times 10''$ at position angle $PA = 118^\circ$, excluding the central circle of D1 and interior point sources.

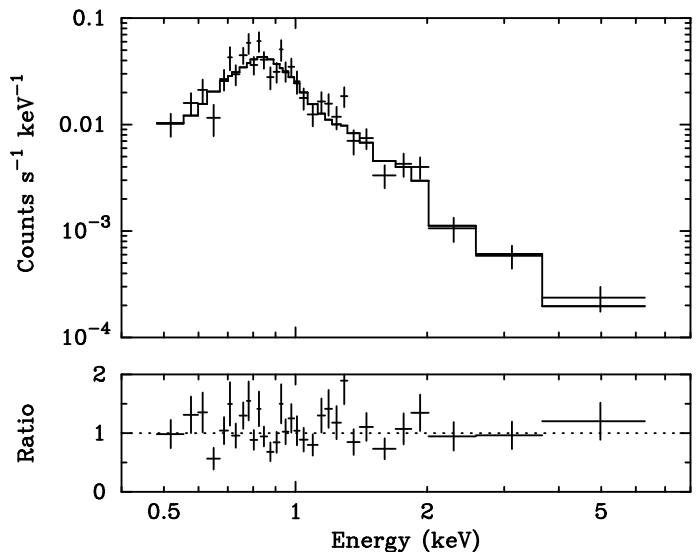


FIG. 8.— *Chandra* ACIS-S3 spectrum of central diffuse emission (region D1). A thermal component and a power law are required to fit the data.

We fit D1 with an absorbed thermal component and a power law (Figure 8, Table 1). For the thermal emission, $kT = 0.63 \text{ keV}$, and the power-law photon index $\Gamma = 2.2$. With the total column density the same for all components and a free parameter, we find $N_H = 8.4 \times 10^{20} \text{ cm}^{-2}$ in the best-fitting model, but it is not significantly different from the Galactic contribution alone, of $N_{H,MW} = 4.7 \times 10^{20} \text{ cm}^{-2}$. The thermal plasma accounts for most of the soft X-rays, and the power law is responsible for nearly all the hard X-rays. Spectrally, the extended central region is very similar to the southern central source, although it has a much lower surface brightness. The ratio of hard to soft luminosity is somewhat larger in D1, compared with the southern source. In this case, normal disk sources, in addition to those in the areas of significant star formation, likely become increasingly important.

We considered abundance variations in the D1 spectrum but found no evidence for non-solar abundances. Similar to the results of the South region, excluding the non-thermal component cannot reproduce the higher-energy spectrum of D1, even using multi-temperature, variable abundance models.

The spectrum of the largest region, D2, also requires a single-temperature plasma. This component is much

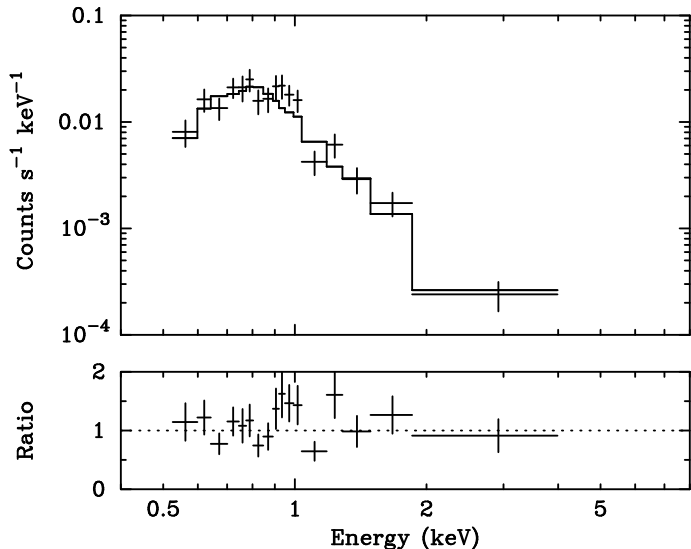


FIG. 9.— *Chandra* ACIS-S3 spectrum of very extended diffuse emission (region D2). A single thermal component and power law fit the data.

cooler ($kT = 0.25$ keV) and more absorbed ($N_H = 4.2 \times 10^{21} \text{ cm}^{-2}$). The required second component is not well constrained. We model it as a power-law, fixing $\Gamma = 2.2$, the best-fitting value of Γ in the D1 spectrum. The best-fitting model of D2 is plotted with the spectrum in Figure 9, and the model parameters are listed in Table 1.

A multi-temperature medium may be a more accurate description of physical conditions of this region, possibly accounting for the unphysical conclusion that this region is more obscured than D1. With the limited sensitivity of these data, however, more complex models are not statistically significant. Examining a model that includes a second thermal plasma component, we find $kT_2 \approx 0.9$ keV. With this higher-temperature component accounting for the $E \approx 1$ keV emission, the normalization of the very soft component is lower. The column density is also slightly lower ($N_H = 3.1 \times 10^{21} \text{ cm}^{-2}$), although still larger than that measured in D1.

4.4. Additional Sources

We detect several other weaker sources within $2'$ of the center of NGC 5135, which we list in Table 2 in order of distance from the nucleus. The last three are unlikely to reside within the galaxy, but we include them for completeness, since they are located within a few arcseconds of the optically-detected spiral arms. These additional sources are interesting as possible intermediate-luminosity X-ray objects (IXOs), those with X-ray luminosity $L_X > 10^{39} \text{ erg s}^{-1}$. Exceeding the Eddington luminosity of a stellar-mass black hole, they could be single sources if they are more massive, accrete above the Eddington rate, or emit anisotropically. Although IXOs are observed in galaxies without intense ongoing star formation (Colbert & Ptak 2002), in galaxies having high star formation rates, a significant population of IXOs is correlated with the star formation rate (Colbert et al. 2003). Not all of the sources listed in Table 2 are intermediate-mass (10^2 – $10^5 M_\odot$) black hole candidates, however. Four of the NGC 5135 sources (2, 3, 5, and 6) are certainly spatially extended, and even the unresolved sources en-

compass spatial scales of several hundred parsecs, so they could be clusters of multiple sources.

The net source counts in the total (0.3–8 keV), soft (0.3–2 keV), and hard (2–8 keV) bands are listed in columns 4 through 6, respectively, where the local background measured in a surrounding annulus has been subtracted. We use these energy bands, rather than the 0.5–2 and 2–10 keV that are more common in the literature and presented elsewhere in this work to avoid errors in the model-dependent conversion of the observed data to unmeasured energies. In some cases, the total number of background-subtracted counts detected does not equal the sum of the soft- and hard-band measurements because of rounding errors. None of the sources is bright enough to distinguish the true physical character of its emission, but soft and hard count rates indicate variations of spectral hardness in the different sources. We note that many of these sources are extremely soft, unlike the harder emission typically measured in IXOs. The emission of these soft sources could therefore be thermal, due to concentrations of supernovae and stellar outflows, although we cannot rule out accretion, which produces soft spectra in some IXOs (Terashima & Wilson 2003).

To estimate fluxes and luminosities consistently, we model each spectrum as an absorbed power law, even though this may not be physically appropriate. We fix the photon index $\Gamma = 1.8$, and allow absorption to vary in excess of the Galactic column density along this line of sight. The observed fluxes and luminosities (not corrected for absorption) in the 0.3–8 keV band are listed in columns 7 and 8 of Table 2, where the luminosity is calculated for the 59 Mpc distance to NGC 5135.

5. PHYSICAL INTERPRETATION

5.1. Identification of X-ray Emission Sources

The X-ray spectral and spatial information together identify the northern source as the AGN of NGC 5135. The most compelling evidence is the Fe $K\alpha$ line, which stellar processes cannot produce with such a large luminosity or equivalent width. The spectral aperture by necessity covers a relatively large area, so in addition to the AGN, it includes other emission sources. Therefore, the energy-restricted Fe-line image is required to spatially constrain the AGN. In this uncontaminated image of the central engine, we demonstrate that the AGN is unresolved.

At higher spatial resolution, we also identify the AGN located north of extended stellar emission in *Hubble Space Telescope* (*HST*) optical and near-infrared (NIR) images. NGC 5135 was observed for 500s with the Wide-Field and Planetary Camera 2 (WFPC2) through the F606W filter on 1995 February 15 and for 320s with NICMOS Camera 2 through the F160W filter on 1998 May 28. In both the optical and NIR, the nucleus is located at the apparent center of relatively bright emission that extends over scales of $5''$. In the latter, at $1.6\mu\text{m}$, it is unresolved and the brightest source. In the former, the nuclear emission is resolved, including a significant contribution that extends over physical scales greater than 10 pc. The strongly-obscured AGN is not the brightest source observed within the 606W filter bandpass. In the ultraviolet, the AGN is a weak source compared with nearby stellar emission, as observed at 2150\AA with the F210M filter of *HST*'s Faint Object

TABLE 2. ADDITIONAL SOURCES

Source	R.A. (J2000)	Decl. (J2000)	Counts (0.3-8 keV)	Counts (0.3-2 keV)	Counts (2-8 keV)	$F_{0.3-8}$ (10^{-15} erg cm $^{-2}$ s $^{-1}$)	$L_{0.3-8}$ (10^{39} erg s $^{-1}$)
1	13 25 43.7	-29 49 56	46	43	3	7.7	3.2
2	13 25 44.7	-29 50 04	41	26	15	7.5	3.2
3	13 25 44.8	-29 50 14	25	20	4	6.0	2.5
4	13 25 42.6	-29 50 06	13	13	0	6.4	2.7
5	13 25 45.3	-29 50 08	20	14	5	4.9	2.1
6	13 25 45.2	-29 50 12	8	7	0	3.6	1.5
7	13 25 44.1	-29 49 33	8	7	1	2.7	1.1
8	13 25 45.3	-29 49 35	6	5	1	1.9	0.80
9	13 25 48.0	-29 49 48	35	31	5	11	4.6
10	13 25 46.7	-29 51 43	9	7	2	0.98	0.41
11	13 25 44.1	-29 48 10	68	46	22	13	5.5
12	13 25 52.8	-29 50 09	30	25	10	5.4	2.3

NOTE. — Units of right ascension are hours, minutes, and seconds, and units of declination are degrees, arcminutes, and arcseconds.

Camera for 1963s on 1995 July 17. (We note that the AGN is located approximately $0''.2$ west and $1''.7$ north of the UV-brightest point and is *not* the location that González Delgado et al. (1998) tentatively identified as the nucleus. In fact, their UV spectral aperture probably excluded most of the AGN light.)

Because of errors in the absolute astrometry of both *Chandra* and *HST*, the location of the northern X-ray source does not appear to be exactly coincident with the UV, optical, or NIR AGN, based on the telescopes' reported astrometry alone. In Figure 10, we illustrate the approximate relationship between the X-ray and optical emission, having shifted the X-ray contours by $1''.8$ to align the northern source with the optical AGN and re-sampled onto a common pixel scale. A further clockwise rotation of the X-ray image may also be suggested, but the simple planar shift alone illustrates the strong stellar contribution south of the AGN, near the southern X-ray source.

The AGN is not the only source of X-ray emission within the 340-pc northern spectral aperture. Mass is strongly concentrated in the nuclear region, so it is a location of the most intense star formation. At the higher resolution of WFPC2, we distinguish many individual stellar sources at optical wavelengths on sub-arcsecond scales. Stellar processes, including supernovae, stellar winds, and large-scale outflows, are likely responsible for the soft thermal X-ray emission, even in the immediate surroundings of the AGN. Most of the thermal emission in the northern region is due to the 0.6-keV component, which is similar to the only significant thermal components of the South and D1 regions. Thus, we suggest that even within the northern aperture, the thermal emission is stellar, not due to the AGN.

At 6 cm, VLA observations show concentrated emission at $\alpha = 13^{\text{h}}25^{\text{m}}43.^{\text{s}}94$, $\delta = -29^{\circ}50'02''.8$ (J2000), with some low-level emission extending toward the northeast (Ulvestad & Wilson 1989). The radio core appears to be offset $2''.9$ south of the AGN, which is located in the continuum-subtracted Fe K α image at $\alpha = 13^{\text{h}}25^{\text{m}}43.^{\text{s}}97$, $\delta = -29^{\circ}50'00''.0$ (J2000). The radio core appears aligned instead with the southern X-ray source (within $0''.3$), suggesting that the concentrated radio emission is due to the starburst.

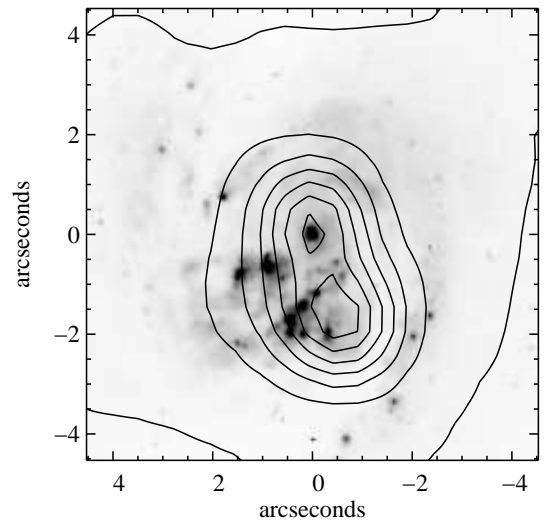


FIG. 10.— *HST* optical (6060Å) image with *Chandra* total-band contours overlaid, scaled linearly. North is up and east is to the left. The AGN is located at the origin, with the X-ray emission shifted to align at the northern X-ray source. In both images, the AGN is north of prominent, extended emission. The high-resolution optical data also illustrate that stellar sources, in addition to the AGN, are contained within the small nuclear X-ray aperture.

The southern source is simply a starburst. The thermal emission and the hard continuum are typical spectral components measured in local starbursts. The power-law continuum in the starburst region is therefore unrelated to the nearby AGN in this galaxy. Although only one thermal component is significant in this region, the reality is likely more complicated, with a range of temperatures actually present (Strickland & Stevens 2000).

The starburst is viewed approximately face-on. The southern X-ray extraction includes most of the high surface brightness region measured in the UV continuum (González Delgado et al. 1998). Edge-on starbursts, such as M82 and NGC 253, indicate the three-dimensional structure that the aperture covers (Strickland et al. 2003). Specifically, the X-ray- and UV-brightest regions of intense star formation are located

at the base of an outflowing superwind, which extends conically out of the plane of the galaxy. The 0.7-keV thermal component is most similar to the diffuse outflow measured in the edge-on cases, where it can be spatially isolated. The 200-pc radial scale of NGC 5135's bright starburst is comparable to the intense cores of edge-on starbursts, so we expect that the outflow extends on similar physical scales—on the order of a kpc or two—along the line of sight.

The diffuse region D1 is spectrally similar to the intense starburst, with the same hard power-law and soft thermal components, although at greatly diminished surface brightness. These two regions may be genuinely related, representing the outer walls of the expanding conical outflow, which is projected onto the starburst base at small scale height and has a larger projected radius at large scale height. The more extended component, D2, arises in the larger (4 kpc scale) star-forming area that the optical and UV *HST* images show, but X-ray emission does not cover the entire galaxy disk. Thus, even this extended component is closely tied to the sites of significant star formation, so this diffuse emission is most likely a halo rather than disk component of NGC 5135's interstellar medium.

5.2. Fluorescent Iron Emission

The properties of the Fe line measured in the AGN spectrum are consistent with fluorescence in a cold, “neutral” medium. The spectrally unresolved line limits the temperature to $T < 2 \times 10^6$ K. The energy of Fe $K\alpha$ is about 6.4 keV for all ions up to Fe XVII, and only reaches 6.7 and 6.9 keV for He-like and H-like Fe, respectively. Thus, the Fe line we observe in NGC 5135 is not broad or ionized enough to arise in a scattering medium that views the intrinsic continuum directly. In these more sensitive and higher resolution data, we do not find any evidence for the strong ionized Fe lines reported by Turner et al. (1997) based on *ASCA* observations. The hard X-ray fluxes of these two observations separated by over 5 years are similar, so AGN variability is an unlikely explanation for this discrepancy.

The large fluorescent iron equivalent width, $EW = 2.4$ keV, further constrains the geometry of material close to the AGN. In the simplest case, where both the continuum and Fe lines are viewed directly, $EW \lesssim 250$ eV (Krolik & Kallman 1987), which is typical of Seyfert 1 galaxies (e.g., Nandra & Pounds 1994). Reaching $EW > 1$ keV requires high column density ($N_H > 10^{24} \text{ cm}^{-2}$) in the fluorescing region (Ghisellini, Haardt, & Matt 1994; Krolik et al. 1994).

Detection of an extremely large EW strongly constrains the geometry of the obscurer. Extending the simulations of Krolik et al. (1994), Levenson et al. (2002) show that variations of geometry, not iron abundance or intrinsic spectral shape, are required to produce EWs significantly greater than 1 keV. Specifically, the largest EWs require that the solid angle covering fraction of the AGN is also large. Equivalently, we may describe this situation as a small opening angle of a toroidal obscuring region. In NGC 5135, for example, the measured EW constrains the opening angle, $\theta \leq 20^\circ$, or covering fraction $\geq 90\%$. Figure 11 illustrates the effect of variations of θ and Thomson optical depth along the line of sight, τ , on the EW. The Fe $K\alpha$ EW measured in NGC 5135

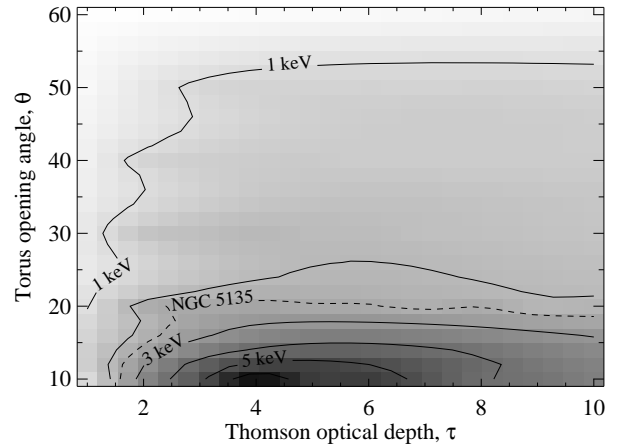


FIG. 11.— Fe $K\alpha$ line EW as a function of Thomson optical depth and opening angle of the obscuring region (Krolik et al. 1994; Levenson et al. 2002). The extremely large EW of NGC 5135 (dashed line) requires an opening angle $\theta \leq 20^\circ$, or equivalently a covering fraction $\geq 90\%$.

is also plotted.

The large covering fraction may be related to the circumnuclear starburst in this case. The mechanical energy of stellar winds and supernovae may help to “puff” the obscuring torus of material to become more spherical than disk-like. Whatever the origin, the large covering fraction means that very few lines of sight to this galaxy have a direct view of the central engine. Galaxies similar to NGC 5135 are therefore extremely unlikely to be observed as Seyfert 1s.

The luminosity of the $K\alpha$ line is related to the intrinsic luminosity of the AGN, although the uncertainty in the exact correlation is large. Based on the $K\alpha$ luminosity, we estimate the intrinsic 2–10 keV luminosity of the AGN $L_{2-10,int} = 1 \times 10^{43} \text{ erg s}^{-1}$, considering opening angles $\theta \leq 20^\circ$ in the Monte Carlo simulations of Krolik et al. (1994) and Levenson et al. (2002). As expected in this Compton thick AGN, less than 1% of the intrinsic X-ray luminosity emerges from the obscured region at hard X-ray energies; the observed 2–10 keV luminosity, $L_{2-10,AGN} = 3 \times 10^{40} \text{ erg s}^{-1}$. Scaling the predicted intrinsic hard X-ray luminosity to the observed spectral energy distributions of unobscured quasars (Elvis et al. 1994), we estimate the bolometric luminosity of the AGN below 10 keV; $L_{bol,AGN} = 3 \times 10^{44} \text{ erg s}^{-1}$, which is only half of the bolometric luminosity of the galaxy as a whole (§6).

5.3. Absorption and Geometry

Along the direct line of sight to the AGN we find $N_H > 10^{24} \text{ cm}^{-2}$, based on the large Fe $K\alpha$ EW and the absence of a continuum characteristic of a directly-viewed AGN, even at hard X-ray energies. The optical [O III] $\lambda 5007$ luminosity relative to the 2–10 keV emission offers further support for the Compton thick classification of NGC 5135. The [O III] emission is expected to arise outside the obscuring region, while the emergent X-ray continuum may be suppressed along the line of sight. A ratio $L_{2-10}/L_{[O III]} < 1$ is characteristic of Compton thick cases (Maiolino et al. 1998). In a 2–4'' aper-

TABLE 3. REGION LUMINOSITIES

Region	$L_{0.5-2}$ (10^{40} erg s $^{-1}$)	L_{2-10} (10^{40} erg s $^{-1}$)
NGC 5135 (total)	18	19
North (AGN)	2.6	9.4
South (SB)	4.6	1.5
D1	3.1	1.6
D2	1.5	0.5

ture, Whittle (1992) measures a flux $f_{[\text{O III}]} = 2.2 \times 10^{-13}$ erg cm $^{-2}$ s $^{-1}$. Correcting for reddening based on the Balmer decrement (González Delgado et al. 1998), we find $L_{2-10}/L_{[\text{O III}]} = 0.08$. Starburst emission certainly contributes to the measured [O III] luminosity, but this result is at least consistent with Compton thick obscuration of the AGN.

The starburst itself is responsible for some of this obscuration. In general, the circumnuclear starburst requires a concentration of mass, some of which is located in front of the active nucleus. In this case, we use the star formation rate measured within the $1''.7 \times 1''.7$ aperture of the Goddard High Resolution Spectrograph (GHRS) on *HST* to estimate the column density near the nucleus. A star-formation rate $SFR \approx 2 M_{\odot} \text{ yr}^{-1}$ (González Delgado et al. 1998) within this aperture corresponds to a mean gas column density $N_H \approx 10^{23} \text{ cm}^{-2}$, using the conversion of Kennicutt (1998). In extreme star-forming galaxies, such as Arp 220, the observed SFR alone produces Compton thick column densities along the line of sight.

We find slightly lower column densities in the *Chandra* observations of the starburst areas, including the soft thermal emission in the North region, because we do not directly probe the line of sight to the very center of NGC 5135. We do, however, always measure absorption in excess of the Galactic column density alone. The X-ray measured obscuration, $N_H = 4 \times 10^{21} \text{ cm}^{-2}$, is greater than that measured within the starburst itself in the UV, where $E(B - V) = 0.20$, or $N_H = 1.2 \times 10^{21} \text{ cm}^{-2}$ in the comparable GHRS aperture. The UV extinction relies on modelling the observed emission features assuming a foreground screen, and therefore represents only a lower limit on the total extinction through the entire starburst region. Sources located at $\tau \lesssim 1$ dominate the observed emission. Thus, it is not surprising that the detected AGN, located behind the entire obscuring starburst, is even more absorbed than the thermal emission alone, or that the UV measurement yields a smaller column density. The UV-determined extinction is comparable to the obscuration measured in the X-ray spectrum of region D1. The column density of the D2 extraction is greater. We note that in other UV spectra, González Delgado et al. (1998) also measure greater obscuration in larger apertures in NGC 5135 and other Seyfert 2/starburst galaxies.

6. FAR-INFRARED RELATIONS AND SPECTRAL ENERGY DISTRIBUTIONS

NGC 5135 is classified as a normal Seyfert 2 galaxy on the basis of optical emission-line ratios, yet at most wavelengths, the AGN contributes only a small fraction

of the detectable luminosity. Even in X-rays, the starburst is significant. Table 3 lists the soft and hard X-ray luminosities of the four spectroscopic regions and a $1'$ aperture, which represents the total emission of NGC 5135.

The far-infrared (FIR) emission of NGC 5135 is characteristic of star-forming galaxies, both in spectral shape and relative magnitude. While active galaxies typically exhibit 25- to 60- μm flux ratios $f_{25}/f_{60} > 0.26$ (de Grijp, Lub, & Miley 1987) in the arcminute-scale apertures of the *Infrared Astronomical Satellite* (*IRAS*), $F_{25}/F_{60} = 0.14$ in NGC 5135. The FIR luminosity $L_{\text{FIR}} = 5.5 \times 10^{44} \text{ erg s}^{-1}$, and the total 8–1000 μm luminosity $L_{\text{IR}} = 7.1 \times 10^{44} \text{ erg s}^{-1}$, following the prescriptions of Helou, Soifer, & Rowan-Robinson (1985) and Sanders & Mirabel (1996) to calculate these luminosities from *IRAS* fluxes. For starburst galaxies, $L_{\text{bol}} \approx L_{\text{IR}}$, and in this case, the observed IR luminosity is more than twice the predicted intrinsic luminosity of the buried AGN.

The bolometric luminosity is related to the star formation rate, with $SFR = L_{\text{bol}}/2.8 \times 10^{43}$ (Leitherer & Heckman 1995). Here we find $SFR = 25 M_{\odot} \text{ yr}^{-1}$. As expected, this is greater than the UV SFR measured within the central 500-pc GHRS aperture. It is less than the extinction-corrected $SFR \approx 50 M_{\odot} \text{ yr}^{-1}$ derived from the *International Ultraviolet Explorer* (*IUE*) data (González Delgado et al. 1998), but because the correction for extinction is highly uncertain and large, UV- and IR-measured SFR s often disagree (Meurer, Heckman, & Calzetti 1999).

The ratios of total X-ray to FIR luminosity measured in NGC 5135 are characteristic of starburst galaxies, not AGN. In Seyfert 1 and Seyfert 2 galaxies that do not contain starbursts, $L_{2-10}/L_{\text{FIR}} \geq 10^{-2}$, while this ratio tends to be much lower in starburst and ultraluminous infrared galaxies (Levenson et al. 2001a; Ptak et al. 2003). We find $L_{2-10, \text{total}}/L_{\text{FIR}} = 4.8 \times 10^{-4}$ in NGC 5135, where $L_{2-10, \text{total}}$ is the total observed 2–10 keV luminosity. Considering only the non-AGN contribution, which we take to be the North region contribution subtracted from the total, $L_{2-10, \text{SB}}/L_{\text{FIR}} = 2.4 \times 10^{-4}$, exactly the linear relationship Ranalli, Comastri, & Setti (2003) fit to a local sample of starburst galaxies. The soft X-ray/FIR ratios of NGC 5135 ($L_{0.5-2, \text{total}}/L_{\text{FIR}} = 4.6 \times 10^{-4}$ and $L_{0.5-2, \text{SB}}/L_{\text{FIR}} = 3.9 \times 10^{-4}$) are slightly higher than the starburst average, but within the typical scatter of the data.

Figure 12 illustrates the spectral energy distributions (SEDs) of extended emission and the AGN separately. Across the spectrum, NGC 5135 as a whole (plotted with open circles) appears most similar to dusty starburst galaxies, whose average SED (Schmitt et al. 1997) is plotted, scaled to the luminosity of NGC 5135. Here we estimate the average X-ray SED from the FIR measurements using the relationship of Ranalli et al. (2003). The large-aperture data are compiled from the *IRAS* Faint Source Catalog, ground-based observations of Glass & Moorwood (1985), and *IUE* measurements of Storchi-Bergmann, Kinney, & Challis (1995). The “extended” X-ray data that are indicated at low spectral resolution come from the measurements of the entire galaxy *excluding* the central $2''.5$. (This excluded region,

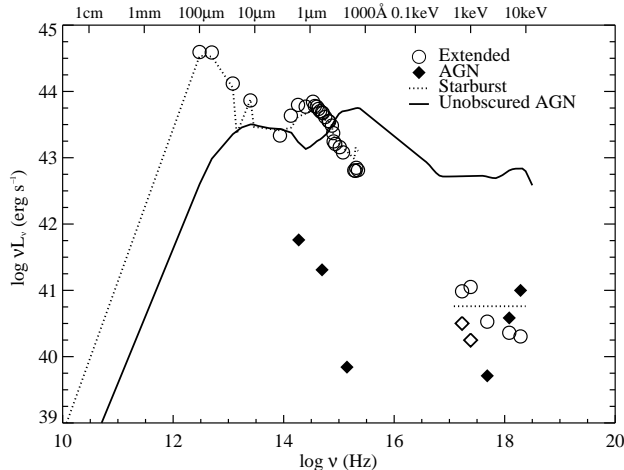


FIG. 12.— Spectral energy distribution of NGC 5135, showing large-scale emission (open circles) and the spatially isolated AGN contributions (filled diamonds). Thermal contributions to the nuclear X-ray spectrum are marked separately (open diamonds). In general, the galaxy appears very similar to dusty starburst galaxies (dotted line; Schmitt et al. 1997). For comparison, the average radio-quiet quasar spectrum (Elvis et al. 1994) scaled to the intrinsic bolometric luminosity of NGC 5135 is shown (solid line). Simple foreground extinction of this spectrum cannot reproduce the unresolved emission. The emergent X-ray spectrum is strongly absorbed and reprocessed, and the SED near optical wavelengths indicates the presence of some additional foreground extinction.

slightly larger than the AGN aperture, was selected to avoid all AGN contamination.) The solid filled X-ray points are measured in the North region and include only the spectral components characteristic of the AGN. The data points are derived from monochromatic fluxes. The highest energy data plotted (at 5 and 8 keV) indicate continuum flux only and exclude the Fe K α line. The open diamonds represent the thermal emission measured in the nuclear region, which we do not attribute immediately to the AGN.

In the UV, optical, and NIR, we measure the AGN alone by fitting the appropriate two-dimensional point-spread function (PSF) to images from the *HST* observations mentioned above. We modeled the optical and NIR PSFs with Tiny Tim⁸ and used the observation of a point source for an empirical UV PSF. The formally best-fitting PSF subtraction within a limited area produces unphysical residuals that decline toward the center and therefore yields an upper limit on the unresolved emission (Ridgway & Stockton 1997). We constrain the residuals (which represent genuinely extended emission) to be monotonic across small interior regions for a more realistic estimate of the AGN contribution. This constraint reduces the AGN flux by about 10% in the NIR and 25% in the optical. It is most restrictive in the UV, where the truly unresolved emission appears to be only one-third of the flux within the central region. For the unresolved emission, we find 6.7×10^{-3} , 9.0×10^{-5} , and 1.1×10^{-6} Jy in the NIR, optical, and UV, respectively.

Where the AGN can be spatially isolated, its spectral energy distribution does not match that of observed radio-quiet quasars (Elvis et al. 1994). A simple screen

of obscuration in the foreground of the average unobscured quasar also fails to describe the AGN SED. The Compton thick reprocessing, which strongly alters the X-ray spectrum, is essential. Although spatially unresolved, the observed lower-energy emission must also be reflected; we would not detect the AGN directly at these wavelengths behind a column density of 10^{24} cm^{-2} . The steep decline of the relative luminosity from the NIR through UV, however, indicates that some additional foreground obscuration is also present.

This example illustrates the difficulty of identifying an AGN in the presence of a starburst, especially more distant cases where spectral apertures cover larger physical scales and signal-to-noise ratios are diminished. The characteristic optical emission lines are easily diluted when off-nuclear sources account for a larger fraction of the light (Moran, Filippenko, & Chornock 2002; Kauffmann et al. 2003), or when a strong starburst is also present (Levenson et al. 2001b).

Only above 4 keV does the AGN dominate the detectable emission from NGC 5135, yet simple modeling of the total X-ray spectrum would yield misleading results. The detected 2–10 keV luminosity could be produced by a starburst alone. The spatially-integrated spectrum is relatively flat from 0.4–8 keV, offering no indication of the distinct physical origin of the soft and hard components. The strong obscuration of the AGN is not at all evident in the spatially-integrated spectrum. A crude technique such as spectral hardness ratios would incorrectly suggest the presence of a weak yet unobscured AGN. The example of NGC 5135 demonstrates how such Compton thick AGN may therefore remain successfully hidden at most wavelengths where surveys have been performed, particularly when they are located at large redshift.

Compton thick examples are truly normal AGN, comprising roughly half of samples that are not selected on the basis of their X-ray emission (Risaliti, Maiolino, & Salvati 1999). They do not necessarily appear to be X-ray bright below 10 keV. Stellar processes further complicate their soft X-ray spectra, since the large reservoirs of gas that block the AGN can also form stars, which subsequently produce soft thermal emission.

Though difficult to identify, such obscured sources may contribute significantly to the cosmic X-ray background. Synthesis models that combine a distribution in both absorption to the central engine and redshift (Setti & Woltjer 1989; Madau, Ghisellini, & Fabian 1994; Comastri et al. 1995) are essential to reproduce the background spectrum, which peaks around 30 keV. While discrete sources account for 80% or more of the XRB at energies up to 10 keV (Brandt et al. 2001; Giacconi et al. 2001; Hasinger et al. 2001), these observed redshift and column density distributions do not spectrally match the X-ray background at higher energies (Gilli 2003). Furthermore, theoretical models (Fabian et al. 1998) suggest that up to 90% of the accretion power in the Universe is hidden from direct view. NGC 5135 offers a local demonstration of how such sources may remain effectively buried behind large column densities and along most lines of sight.

⁸ <http://www.stsci.edu/software/tinytim>

In analyzing this *Chandra* ACIS observation of the Seyfert 2/starburst galaxy NGC 5135, we spatially and spectrally distinguish both the AGN and the stellar origin of its X-ray emission. Images reveal two strong and concentrated central sources. The northern of these is the AGN, while the southern is associated with star formation and likely represents the base of an outflowing starburst superwind. Recognizing the contributions of both the AGN and stellar processes, we apply physically-motivated models to spectroscopy of several distinct regions of interest. In addition to the two central sources, these regions include two extended areas, which likely represent a hot halo component of NGC 5135. In the nuclear region, the AGN produces a very flat ($\Gamma = 0$) power law continuum and extremely prominent ($\text{EW} = 2.4 \text{ keV}$) Fe K α fluorescence line. These spectral characteristics demonstrate that the central engine is highly obscured, behind $N_H > 10^{24} \text{ cm}^{-2}$. The intrinsic emission emerges only after being strongly reprocessed and is diminished by factors of 100 as observed in the *Chandra* bandpass. This central region encompasses a physical scale of 340 pc, which includes sites of prominent star formation that are viewed directly in UV through NIR wavelengths. These stars are responsible for the soft thermal emission we measure in this region.

The remainder of the X-ray emission, including the southern source, is spatially resolved. We attribute this emission to star formation. Prominent soft thermal X-rays characterize these spectra. They also require some additional continuum components, which are responsible for their higher-energy ($E > 4 \text{ keV}$) luminosity. Unresolved populations of X-ray binaries likely produce this emission.

The vast majority of the detected soft X-ray luminosity from NGC 5135 ($L_{0.5-2} = 1.8 \times 10^{41} \text{ erg s}^{-1}$) is spatially extended. The southern source accounts for fully one-quarter of this emission. The AGN itself accounts for almost none of it, given that nearly all of the soft X-rays within the nuclear aperture are thermal. The AGN is directly responsible for roughly half the detected hard X-ray luminosity ($L_{2-10} = 1.9 \times 10^{41} \text{ erg s}^{-1}$). Based on the luminosity of the Fe K α line, we estimate the intrinsic bolometric luminosity of the AGN: $L_{\text{bol,AGN}} = 3 \times 10^{44} \text{ erg s}^{-1}$. This AGN luminosity is only half of the bolometric luminosity of the galaxy as a whole, $L_{\text{bol}} \approx 7 \times 10^{44} \text{ erg s}^{-1}$, based on the IR luminosity.

We suggest that the starburst is related to the obscuration of the AGN. The starburst itself directly hides the AGN, at least in part. The measured star formation rate alone can account for 10% of the indicated absorption. A

starburst requires large reservoirs of gas in the center of the galaxy, and the dynamic conditions that concentrate this material also serve to further obscure the AGN. The starburst may also be related to the *activity* of the central engine, with the instabilities that lead to star formation aiding accretion.

Although optically classified as an ordinary Seyfert 2 galaxy, the Fe K α emission is the only X-ray feature that truly identifies the presence of an AGN. The extremely large EW of the line requires a very large (90%) covering fraction of material, allowing few direct views of the central engine from any line of sight. The Compton thick obscuration severely diminishes the hard X-ray emission that is a useful discriminant of less-obscured AGN.

NGC 5135 represents a local case study of some of the complex reality that is also likely present in more distant examples. Even in X-rays, stellar processes are significant, and combined with Compton thick obscuration, a deeply buried AGN will not be obvious in data that have low effective spatial or spectral resolution. These are particular difficulties in the study of ultraluminous infrared galaxies, in which star formation is known to be important, and also in the resolution of the X-ray background, where large obscuration along most lines of sight diminishes the likelihood of identifying the hidden AGN that are essential to produce the background spectrum at higher energies.

We thank B. McKernan for providing XSTAR photoionization models, A. Kinkhabwala for the observed spectrum of NGC 1068, and an anonymous referee for useful suggestions. We thank D. K. Strickland for advice on identifying sources and S. E. Ridgway for many discussions about PSF subtraction. This research has made use of the NASA/IPAC Extragalactic Database (NED) which is operated by the Jet Propulsion Laboratory, California Institute of Technology, under contract with the National Aeronautics and Space Administration. The Digitized Sky Survey was produced at the Space Telescope Science Institute under U.S. Government grant NAG W-2166. The Second Epoch image presented here was made by the Anglo-Australian Observatory with the UK Schmidt Telescope. Part of this work was based on observations made with the NASA/ESA Hubble Space Telescope, obtained from the data archive at the Space Telescope Science Institute. STScI is operated by the Association of Universities for Research in Astronomy, Inc. under NASA contract NAS 5-26555. This work is supported by NASA grant G01-2119.

REFERENCES

- Anders, E., & Grevesse, N. 1989, *Geochim. Cosmochim. Acta*, 53, 197
- Arnaud, K. A. 1996, in ASP Conf. Ser. 101, *Astronomical Data Analysis Software and Systems V*, ed. G. Jacoby & J. Barnes (San Francisco: ASP), 17
- Arnaud, M., & Rothenflug, M. 1985, *A&AS*, 60, 425
- Boller, T., Keil, R., Hasinger, G., Costantini, E., Fujimoto, R., Anabuki, N., Lehmann, I., & Gallo, L. 2003, *A&A*, in press (astro-ph/0307326)
- Brandt, W. N., et al. 2001, *AJ*, 122, 1
- Brinkman, A. C., Kaastra, J. S., van der Meer, R. L. J., Kinkhabwala, A., Behar, E., Kahn, S. M., Paerels, F. B. S., & Sako, M. 2002, *A&A*, 396, 761
- Cash, W. 1979, *ApJ*, 228, 939
- Cid Fernandes, R., Heckman, T. M., Schmitt, H., González Delgado, R. M., & Storchi Bergmann, T. 2001, *ApJ*, 558, 81
- Colbert, E. J. M., Heckman, T. M., Ptak, A. F., Strickland, D. K., & Weaver, K. A. 2003, submitted to *ApJ* (astro-ph/0305476)
- Colbert, E. J. M., & Ptak, A. 2002, *ApJS*, 142, 25
- Comastri, A., Setti, G., Zamorani, G., & Hasinger, G. 1995, *A&A*, 296, 1
- Dahlem, M., Weaver, K. A., & Heckman, T. M. 1998, *ApJS*, 118, 401
- Dahlem, M., Parmar, A., Oosterbroek, T., Orr, A., Weaver, K. A., & Heckman, T. M. 2000, *ApJ*, 538, 555
- de Grijp, M. H. K., Lub, J., & Miley, G. K. 1987, *A&AS*, 70, 95
- Elvis, M., et al. 1994, *ApJS*, 95, 1

- Fabian, A. C., Barcons, X., Almaini, O., & Iwasawa, K. 1998, *MNRAS*, 297, L11
- Ferrarese, L., & Merritt, D. 2000, *ApJ*, 539, L9
- Gebhardt, K., et al. 2000, *ApJ*, 539, L13
- Ghisellini, G., Haardt, F., & Matt, G. 1994, *MNRAS*, 267, 743
- Giacconi, R., et al. 2001, *ApJ*, 551, 624
- Gilli, R. 2003, *Adv. Sp. Res.*, in press (astro-ph/0303115)
- Glass, I. S., & Moorwood, A. F. M. 1985, *MNRAS*, 214, 429
- González Delgado, R. M., Heckman, T., Leitherer, C., Meurer, G., Krolik, J., Wilson, A. S., Kinney, A., & Koratkar, A. 1998, *ApJ*, 505, 174
- Hasinger, G., et al. 2001, *A&A*, 365, L45
- Helou, G., Soifer, B. T., & Rowan-Robinson, M. 1985, *ApJ*, 298, L7
- Kauffman, G., et al. 2003, *MNRAS*, in press (astro-ph/0304239)
- Kennicutt, R. C. 1998, *ApJ*, 498, 541
- Kinkhabwala, A. et al. 2002, *ApJ*, 575, 732
- Krolik, J. H., & Kallman, T. R. 1987, *ApJ*, 320, L5
- Krolik, J. H., Madau, P., & Życki, P. T. 1994, *ApJ*, 420, L57
- Leitherer, C., & Heckman, T. M. 1995, *ApJS*, 96, 9
- Levenson, N. A., Cid Fernandes, R., Jr., Weaver, K. A., Heckman, T. M., & Storchi-Bergmann, T. 2001b, *ApJ*, 557, 54
- Levenson, N. A., Krolik, J. H., Życki, P. T., Heckman, T. M., Weaver, K. A., Awaki, H., & Terashima, Y. 2002, *ApJ*, 573, L81
- Levenson, N. A., Weaver, K. A., & Heckman, T. M. 2001a, *ApJ*, 550, 230
- Liedahl, D. A. 1992, Ph.D. Dissertation, University of California, Berkeley
- Madau, P., Ghisellini, G., & Fabian, A. C. 1994, *MNRAS*, 270, L17
- Magdziarz, P. & Zdziarski, A. A. 1995, *MNRAS*, 273, 837
- Maiolino, R., Salvati, M., Bassani, L., Dadina, M., della Ceca, R., Matt, G., Risaliti, G., & Zamorani, G. 1998, *A&A*, 338, 781
- Martin, C. L., Kobulnicky, H. A., & Heckman, T. M. 2002, *ApJ*, 574, 663
- Matt, G., Fabian, A. C., & Reynolds, C. S. 1997, *MNRAS*, 289, 175
- Meurer, G. R., Heckman, T. M., & Calzetti, D. 1999, *ApJ*, 521, 64
- Mewe, R., Gronenschild, E. H. B. M., & van den Oord, G. H. J. 1985, *A&AS*, 62, 197
- Mewe, R., Lemen, J. R., & van den Oord, G. H. J. 1986, *A&AS*, 65, 511
- Moran, E. C., Filippenko, A. V., & Chornock, R. 2002, *ApJ*, 579, L71
- Nandra, K., & Pounds, K. A. 1994, *MNRAS*, 268, 405
- Phillips, M. M., Charles, P. A., & Bladwin, J. A. 1983, *ApJ*, 266, 485
- Ptak, A., Heckman, T., Levenson, N. A., Weaver, K., & Strickland, D. 2003, *ApJ*, 592, 782
- Ranalli, P., Comastri, A., & Setti, G. 2003, *A&A*, 399, 39
- Ridgway, S. E., & Stockton, A. 1997, *AJ*, 114, 511
- Risaliti, G., Maiolino, R., & Salvati, M. 1999, *ApJ*, 522, 157
- Sanders, D. B., & Mirabel, I. F. 1996, *ARA&A*, 34, 749
- Schmitt, H. R., Kinney, A. L., Calzetti, D., & Storchi Bergmann, T. 1997, *AJ*, 114, 592
- Setti, G., & Woltjer, L. 1989, *A&A*, 224, L21
- Storchi-Bergmann, T., Kinney, A. L., & Challis, P. 1995, *ApJS*, 98, 103
- Strickland, D. K., Heckman, T. M., Colbert, E. J. M., Hoopes, C. G., & Weaver, K. A. 2003, submitted to *ApJS* (astro-ph/0306592)
- Strickland, D. K., Heckman, T. M., Weaver, K. A., Hoopes, C. G., & Dahlem, M. 2002, *ApJ*, 568, 689
- Strickland, D. K., & Stevens, I. R. 2000, *MNRAS*, 314, 511
- Terashima, Y., & Wilson, A. S. 2003, *ApJ*, in press (astro-ph/0305563)
- Turner, T. J., George, I. M., Nandra, K., & Mushotzky, R. F. 1997, *ApJS*, 113, 23
- Ulvestad, J. S., & Wilson, A. S. 1989, *ApJ*, 343, 659
- Weisskopf, M. C., Tananbaum, H. D., Van Speybroeck, L. P., & O'Dell, S. L. 2000, *Proc. SPIE*, 4012, 2
- Weaver, K. A., Heckman, T. M., Strickland, D. K., & Dahlem, M. 2002, *ApJ*, 576, L19
- Weaver, K. A., Heckman, T. M., & Dahlem, M. 2000, *ApJ*, 534, 684
- Whittle, M. 1992, *ApJS*, 79, 49
- Zezas, A., Fabbiano, G., Rots, A. H., & Murray, S. S. 2002, *ApJ*, 577, 710